ADVANCED MATERIALS
www.advmat.de

From Nanoalloy to Nano-Laminated Interfaces for Highly Stable Alkali-Metal Anodes

Parham Pirayesh, Karnpiwat Tantratian, Maedeh Amirmaleki, Feipeng Yang, Enzhong Jin, Yijia Wang, Lyudmila V. Goncharova, Jinghua Guo, Tobin Filleter, Lei Chen, and Yang Zhao**

Metal anodes are considered the holy grail for next-generation batteries because of their high gravimetric/volumetric specific capacity and low electrochemical potential. However, several unsolved challenges have impeded their practical applications, such as dendrite growth, interfacial side reactions, dead layer formation, and volume change. An electrochemically, chemically, and mechanically stable artificial solid electrolyte interphase is key to addressing the aforementioned issue with metal anodes. This study demonstrates a new concept of organic and inorganic hybrid interfaces for both Li- and Na-metal anodes. Through tailoring the compositions of the hybrid interfaces, a nanoalloy structure to nano-laminated structure is realized. As a result, the nanoalloy interface (1Al_2O_3–1alucone or 2Al_2O_3–2alucone) presents the most stable electrochemical performances for both Li-and Na-metal anodes. The optimized thicknesses required for the nanoalloy interfaces for Li- and Na-metal anodes are different. A cohesive zone model is applied to interpret the underlying mechanism. Furthermore, the influence of the mechanical stabilities of the different interfaces on the electrochemical performances is investigated experimentally and theoretically. This approach provides a fundamental understanding and establishes the bridge between mechanical properties and electrochemical performance for alkali-metal anodes.

1. Introduction

The next-generation alkali-metal batteries, such as Li-metal and Na-metal batteries, have received increasing attention because of their high energy densities.[1] However, several challenges need to be addressed before their practical applications. First, the Li- and Na-dendrite growth will induce short circuits and cause safety concerns.[2] Second, undesired chemical and electrochemical side reactions between highly reactive Li/Na metal with liquid electrolytes lead to unstable solid electrolyte interphase (SEI),[3] which results in large polarization and deteriorates the electrochemical performance. Third, the formation of dendrites and unstable SEI lead to low Coulombic efficiency (CE) and inactive "dead Li/Na" layers.[4] A stable SEI enables uniform Li/Na electrochemical deposition behaviors and enhances electrochemical performances. The unstable SEI layer can promote dendrite growth due to the nonuniform ion flux distribution and non-homogeneous alkali-metal depositions, leading to the large polarization and the decay of the electrochemical performances.[5] Various approaches, such as electrolyte modifications, interface engineering, and electrodes/separator designs, have been proposed to stabilize the interface to reduce the dendrite growth, prevent the side reaction and enhance the electrochemical performances.[6] One of the most popular strategies is to design artificial interfaces for Li- and Na-metal anodes.[7] In the

P. Pirayesh, E. Jin, Y. Wang, Y. Zhao
Department of Mechanical and Materials Engineering
University of Western Ontario
London, ON N6A 5B9, Canada
E-mail: yzhao628@uwo.ca

K. Tantratian, L. Chen
Department of Mechanical Engineering
University of Michigan—Dearborn
Dearborn, MI 48128, USA
E-mail: leichn@umich.edu

The ORCID identification number(s) for the author(s) of this article can be found under https://doi.org/10.1002/adma.202301414

DOI: 10.1002/adma.202301414

M. Amirmaleki, T. Filleter
Department of Mechanical and Industrial Engineering
The University of Toronto
Toronto, ON M5S 3G8, Canada

M. Amirmaleki
Department of Materials Science and Engineering
Massachusetts Institute of Technology
Cambridge, MA 02139, USA

F. Yang, J. Guo
Advanced Light Source
Lawrence Berkeley National Laboratory
Berkeley, CA 94720, USA

L. V. Goncharova
Department of Physics and Astronomy
University of Western Ontario
London, ON N6A 3K7, Canada

 © 2023 Wiley-VCH GmbH

previous study, different artificial interfaces have been reported with improved electrochemical performances and reduced dendrite growth, such as ceramic layers, solid-state electrolyte layers, polymer layers, and hybrid layers.[5c,8]

However, a few questions still remain. How do the composition, structure, and properties of the artificial interfaces affect the battery performance? What properties play a major role in cycling stability? For the different alkali metals, will they follow the same design principles for the artificial interfaces? It has been widely studied that the chemical and electrochemical stabilities of the interface can affect electrochemical performances. Recently, the importance of the mechanical properties of the interfaces for the electrochemical deposition behavior and performances is gradually recognized.[9] However, how to design a chemically/electrochemically/mechanically stable interface is still an unanswered question. The most widely used inorganic layers, such as metal oxide or solid-state electrolytes, generally have high Young's modules but are often brittle, which leads to crack formation in the inorganic layers during the metal deposition process.[10] Organic polymers with high flexibility are promising candidates to relieve the volume change of Li/Na metal during cycling.[11] However, the dendrites can penetrate the polymer layers due to their low modulus and strength. In this case, there is still a challenge of balancing the multiple mechanical parameters to achieve a mechanically stable interface.[12] In order to tune the mechanical properties of the interface, the most effective approach is to design the organic and inorganic hybrid structures. The organic-inorganic hybrid layers, with different configurations and compositions, present huge interests as interfacial layers for Li- and Na-metal anodes. Various hybrid structural designs, such as organic-inorganic dual-layer structures, nano-scale gradient structures, cross-linked and multifunctional structures, etc., have been proposed.[9a,13] However, the effects of various hybrid interface structures on electrochemical performance are still being debated. Furthermore, for achieving a long lifetime and dendrite-free structure, there should be a balance between the chemical, electrochemical and mechanical properties of the interfaces.

Different approaches have been reported to fabricate nanohybrid films, such as self-assembly, chemical vapor deposition, and magnetron sputtering, for a diverse range of different applications.[14] However, most of these methods are not suitable for engineering the interface for Li- and Na-metal anode due to the high reactivities and low melting points of alkali metals. Another challenge is to fabricate the hybrid coating with controlled structure and compositions at the nanoscale. Atomic layer deposition (ALD) and molecular layer deposition (MLD) are unique techniques to achieve nano-hybrid interfaces for alkali metals with excellent coverage, conformity, and low deposition temperatures.[15] For example, the elastic modulus of a few nanometers alucone and Al_2O_3 was reported to be 21–37 GPa and ≈165 GPa, respectively. It has also been reported that the ALD-Al_2O_3 and MLD alucone alloy or nano-laminated films with varying ratios of ALD and MLD, lead to the tunable elastic modulus and hardness.[16] The composition of the hybrid film can be controlled by varying the relative number of ALD and MLD cycles. When the number of deposition cycles for ALD and MLD processes are large to deposit full monolayers, it is called a "nano-laminated structure". When both number of ALD and MLD cycles are small, it will generate a homogeneous nano-alloy film.[16c,17] However, there is no demonstration for fabricating the nano-hybrid interfaces with balanced chemical/electrochemical/mechanical properties by tuning the composition of the coating. In addition, the electrochemical metal deposition behavior and performance in different electrolytes are quite different between Li and Na metals. The chemical and physical properties of the different alkali metals may also affect the dendrite formation and electrochemical properties of the interfaces. In this case, the design principles and optimal structures for different alkali metals need to be studied in detail.

Herein, we first propose a new concept of organic and inorganic hybrid interfaces with nanoalloy and nano-laminated structures for Li- and Na-metal anode. First, the structures, thicknesses, and compositions of the hybrid interfaces are precisely controlled by the ALD/MLD process. The structures of nanoalloy to nano-laminated are designed with tuned electrochemical and mechanical properties. Second, the optimized composition and thicknesses of the Al_2O_3–alucone alloy interface on the Li- and Na-metal anodes demonstrate significant enhancement for the electrochemical performances. Third, the surface and interface chemistry of SEI properties and behaviors have been studied in detail by complementary surface and interface characterization techniques. Finally, the mechanisms have been comprehensively understood by the cohesive zone model and phase-field model. Our study provides the bridge between mechanical properties and electrochemical performance for alkali-metal anodes and opens a new window to design the nanostructure interfaces for alkali-metal anodes for the next-generation alkali-metal batteries.

2. Results and Discussion

The schematic diagram of the nano-hybrid interfacial layer is shown in **Figure 1**a. Inorganic ALD-deposited Al_2O_3 and organic MLD-deposited alucone are used to form the nano-hybrid structures, for demonstrating the concept. In this study, two key parameters of the nano-hybrid interface, the unit structures, and thicknesses, are investigated. Three types of unit structures for the nano-hybrid interfaces are fabricated, including one layer of ALD-deposited Al_2O_3 with one layer of MLD-deposited alucone (1ALD-1MLD), two layers of ALD Al_2O_3 with two layers of MLD alucone (2ALD-2MLD), and five layers of ALD Al_2O_3 with another five layers of MLD alucone (5ALD-5MLD). In addition, for each unit structure, different thicknesses have been further investigated by changing the number of deposition cycles. For example, for the 1ALD-1MLD unit structure, we repeat the deposition for this unit structure for a different number of cycles, including 5, 10, and 25 cycles. The corresponding samples for 1ALD-1MLD unit structures with different thicknesses are named: (1ALD-1MLD)5, (1ALD-1MLD)10, and (1ALD-1MLD)25, respectively. The same naming conversion has been applied to the other two types of unit structures. To demonstrate the unique feature of the rational-designed nano-hybrid interface, both Li- and Na-metal anodes are used for comparison.

Several surface characterization methods are applied to understand the surface/ interface compositions of the designed nano-hybrid interfaces for both Li- and Na-metal anodes. The time-of-flight secondary-ion mass spectrometry (TOF-SIMS) is

© 2023 Wiley-VCH GmbH

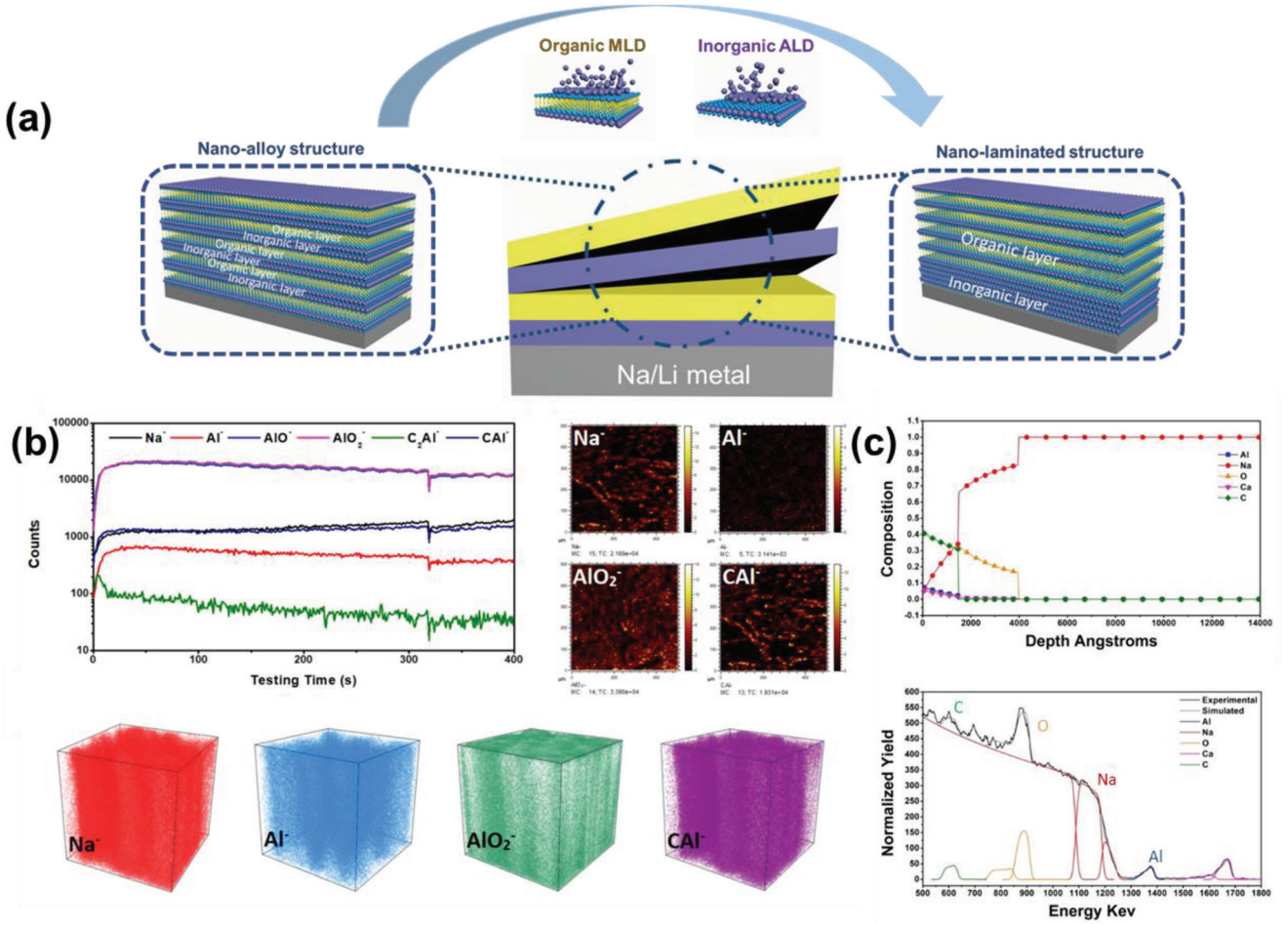

Figure 1. a) Schematic diagram of the fabrication of the nanoalloy and nano-laminated interfacial structures. b) TOF-SIMS secondary-ion images, the depth profile of various secondary ion species and corresponding 3D images of Na@(1ALD-1MLD)10.; c) RBS spectra and calculated depth profiles of Na@(1ALD-1MLD)10.

performed to probe the composition and the element depth distributions of the nano-hybrid. The TOF-SIMS results of Na@(1ALD-1MLD)10, Na@(2ALD-2MLD)4, and Na@(5ALD-5MLD)2 are shown in Figure 1b and Figures S1, S2 (Supporting Information), respectively. Figure 1b presents the TOF-SIMS depth profiles and chemical ion images of Na^-, Al^-, CAl^-, and AlO_2^- species for Na@(1ALD-1MLD)10. Obvious featured species of CAl^-, (from MLD alucone) and Al^-, AlO_2^- (from both ALD Al_2O_3 and MLD alucone) are observed to identify the deposition of the Al-containing film on the substrates of Na metal. From the depth profiles and corresponding 3D images, it can be observed that all of those species of Al^-, CAl^-, and AlO_2^- distribute from the top surface to the bulk Na metals. Similar phenomena can be observed from both Na@(2ALD-2MLD)4 and Na@(5ALD-5MLD)2, in which the ionic species of Al^-, CAl^-, and AlO_2^- distribute along the surface to the bulk Na. The TOF-SIMS results demonstrate that the inorganic-organic alloy structures are successfully deposited by the hybrid ALD-MLD processes.

The Rutherford backscattering spectrometry (RBS) results for Na@(1ALD-1MLD)10, Na@(2ALD-2MLD)4, and Na@(5ALD-5MLD)2 were further performed, as shown in Figure 1c and Figures S3, S4 (Supporting Information). The RBS Al, C and O surface peaks confirm the successful synthesis of the Al-contained hybrid layers on Na metal. According to the elemental depth profiles obtained by simulating RBS spectra, one can observe that the thicknesses of the nano-hybrid layers for three different configurations are very similar, which is ≈200 nm. These results indicate that the sequence of layers of the nano-hybrid structure by ALD/MLD will not affect the total thicknesses of the coating significantly if the total number of ALD-MLD deposition cycles stays the same. Moreover, similar to the TOF-SIMS results, the C spectra from all the samples demonstrate the formation of Al_2O_3–alucone alloy structures, in which the C signals distribute from the top surface to the bulk Na at the same depth as Al.

In addition, the TOF-SIMS results for the nano-hybrid interface coatings on Li metals are shown in Figures S5–S10 (Supporting Information). Figures S5–S7 (Supporting Information) present the top surface secondary ion images and their depth profiles and the corresponding 3D reconstructed images for Li@(1ALD-1MLD)10, Li@(1ALD-1MLD)25, and Li@(1ALD-1MLD)50. For the Li@(1ALD-1MLD)10, the AlC_2^- and $AlOC_2^-$ species derived from MLD alucone distribute along with the

© 2023 Wiley-VCH GmbH

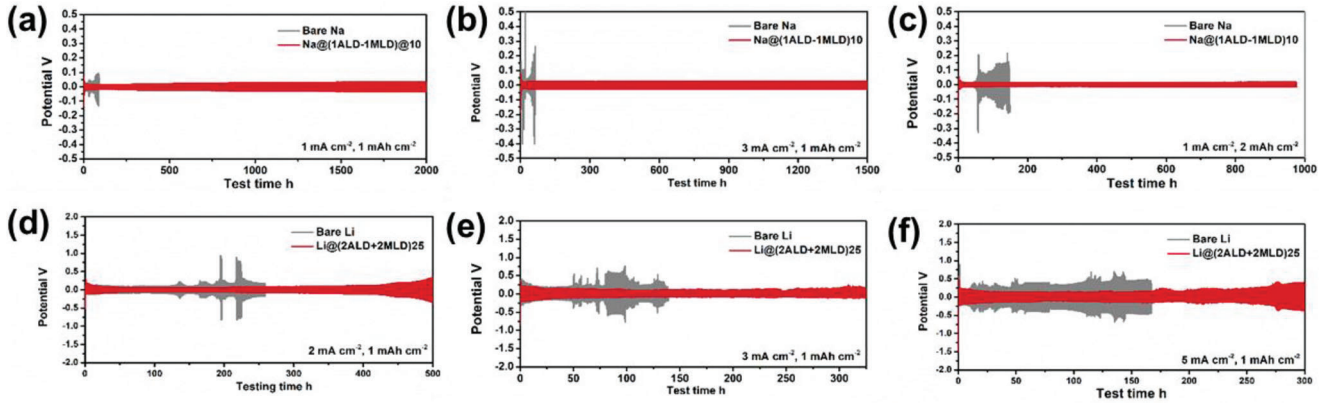

Figure 2. a–c) The electrochemical performances of Na/Na symmetric cells using bare Na foil and Na@(1ALD-1MLD)10 at different current densities and capacities. d–f) The electrochemical performances of Li/Li symmetric cells using bare Li foil and Li@(2ALD-2MLD)25 at different current densities.

AlO^- and AlO_2^- species, which indicates the Al_2O_3–alucone alloy structure and is similar to results for Na@(1ALD-1MLD)10. However, when the total ALD-MLD cycles increase with the same configuration of 1ALD-1MLD (Figures S6, S7, Supporting Information), the signals of AlC_2^- and $AlOC_2^-$ in the depth profiles show fluctuations in the coating layers. The fluctuations of the C-contained species are more obvious for another two configurations of Li@(2ALD-2MLD)25 and Li@(5ALD-5MLD)10, which are shown in Figures S8, S9 (Supporting Information). The fluctuations of the C-contained species indicate the content change of the alucone layer in the coatings and the formation of the Al_2O_3–alucone alloy with more obvious nano-laminated structures. Furthermore, the (10ALD-10MLD)5 are deposited on Li metal and the TOF-SIMS results are shown in Figure S10 (Supporting Information). From the 3D reconstructed images of AlC_2^- for Li@(10ALD-10MLD)5, the clear nano-laminated structure of the C-containing layer is observed, resulting from the MLD alucone deposition. In this case, we found that with the control of the unit structures of ALD-MLD deposition, the compositions of the deposited coatings are precisely controlled from Al_2O_3–alucone alloy to Al_2O_3–alucone nano-laminated structures. With the thin unit structures of 1ALD-1MLD and 2ALD-2MLD, it is difficult to form the nano-laminated layered structures since the thickness of the single ALD and MLD layer is at an angstrom level. The unit structures of 1ALD-1MLD and 2ALD-2MLD are more like the alloy structure with the Al_2O_3–alucone hybrid coatings. However, when we increase the units to 5ALD-5MLD and 10ALD-10MLD, the structures of the coating layers turn into obvious nano-laminated layered structures. In addition, the soft X-ray absorption spectroscopy (XAS) of the near-edge structure at the Al K edge was carried out to further investigate the composition of the designed samples (Figure S11, Supporting Information). As reported in the literature, the main peak for the Al K edge for Al_2O_3 at 1564.7 eV is assigned to transitions from the Al 1s orbitals into Al 3p and O 2p antibonding orbitals of t1u symmetry.[18] In the spectrum for the different compositions, this main peak slightly shifts to the low energy of 1564.4 eV. However, the peaks remain in the same position for the alloy structure (Li@(2ALD-2MLD)25) and the nano-laminated structure (Li@(10ALD-10MLD)5), as shown in Figure S11a (Supporting Information). For the alloy structure of (2ALD-2MLD), the increase of the thicknesses (from 10 cycles to 50 cycles) does not affect the local electronic structures of Al (Figure S11b, Supporting Information).

Symmetrical cells were assembled to evaluate the Na and Li plating/stripping behavior of the different designs of the nano-hybrid layers. Figure S12 (Supporting Information) shows the optimization of the different configurations and thicknesses of the nano-hybrid interfaces for the Na-metal anodes at the current density of 3 mA cm^{-2} with the capacity of 1 mAh cm^{-2}. The electrochemical performances of the unit structure of 1ALD-1MLD with different thicknesses are presented in Figure S12a (Supporting Information). Compared to the performance of bare Na (shown in **Figure 2**b), the Al_2O_3–alucone alloy coating with the unit of 1ALD-1MLD can significantly improve the cycling stability. The optimized thickness of the 1ALD-1MLD unit with the Al_2O_3–alucone alloy structure is Na@(1ALD-1MLD)10. Another two configurations of 2ALD-2MLD and 5ALD-5MLD are investigated under the same conditions, in which the electrochemical performances are presented in Figure S12b,c (Supporting Information), respectively. For the coating with the unit structures of 2ALD-2MLD and 5ALD-5MLD, the thin coatings of Na@(2ALD-2MLD)4 and (5ALD-5MLD)2 show the longest lifetime in their groups. Comparing the various samples with different units and thicknesses, the Na@(1ALD-1MLD)10 with the Al_2O_3–alucone alloy structure presents the best electrochemical performances at the current density of 3 mA cm^{-2} with the capacity of 1 mAh cm^{-2}. The results indicate that with the optimal thickness, the alloy-based interfaces demonstrate better electrochemical performances compared to the nano-laminated layered structural interface for Na-metal anodes.

With the optimized thickness and composition, the Na@(1ALD-1MLD)10 was used to further investigate the battery performance. Figure 2a shows the cycling stability of bare Na foil and Na@(1ALD-1MLD)10 at the current density of 1 mA cm^{-2} with the capacity of 1 mAh cm^{-2}. The initial Na stripping/plating over-potential of bare Na foil is ≈30 mV and rapidly increases to over 100 mV after ≈100 h. Then, the short circuit happens with the sudden drop of the overpotential. In contrast, the initial overpotential of the Na@(1ALD-1MLD)10 is ≈60 mV and it gradually decreases to ≈20 mV after a few cycling, indicating the sodiation process of the Al_2O_3–alucone alloy films. After that, the

 © 2023 Wiley-VCH GmbH

overpotential of Na@(1ALD-1MLD)10 is extremely stable with a low overpotential of 30 mV after ≈2000 h without any short circuit. When the current density is increased to 3 mA cm^{-2} (as shown in Figure 2b), the bare Na even has a faster short circuit within 100 h electrochemical cycling. In comparison, the Na@(1ALD-1MLD)10 displays significantly improved stability with a stable overpotential of 30 mV over 1500 h. We also investigated the electrochemical performance with a higher capacity of 2 mAh cm^{-2} with the current density of 1 mA cm^{-2}, as shown in Figure 2c. The bare Na displays even worse cycling stability at higher capacity with high overpotential and wildly fluctuating curves. Remarkably, the Na@(1ALD-1MLD)10 shows very stable performances with a low overpotential of 30 mV over 1500 h. The electrochemical impedance spectroscopy results for bare Na and Na@(1ALD-1MLD)10 are shown in Figure S13 (Supporting Information) for the Nyquits plots before cycling, after 50 cycles, after 100 cycles, and after longtime cycles under the current density of 3 mA cm^{-2} with the capacity of 1 mA h cm^{-2}. It is considered that two distinct semicircles are associated with both the SEI/electrode (high frequency) and the charge transfer (CT)/electrical double layer (lower frequencies). From Figure S13a (Supporting Information), it can be observed that the resistance of bare Na slightly increases after 50 electrochemical cycles, however, after 100 cycles and long-time cycles, the resistance of bare Na increases rapidly, indicating the serious side reactions, large impedance interface, and dead Na layer formation. As a comparison, the Na@(1ALD-1MLD)10 presents a higher resistance compared to bare Na before cycling, which is consistent with the symmetrical cell performances and due to the non-conductive nature of the Al_2O_3–alucone coating. The resistance of the Na@(1ALD-1MLD)10 after 50 electrochemical plating/stripping decreases and keeps stable after 100 cycles and even after long-time cycling. These results indicate that the Al_2O_3–alucone alloy interlayers have a significant influence on the long-life Na-metal anode. Overall, the Al_2O_3–alucone alloy interface of (1ALD-1MLD)10 demonstrates significantly enhanced electrochemical performances and stabilizes the interfaces with low resistances for Na-metal anode with high current density or high capacity.

To further prove the concept, the Li–Li symmetrical cells were assembled to evaluate the Li plating/stripping behavior in the carbonate-based electrolyte. The thickness of the interface is first optimized using the Al_2O_3–alucone alloy structure of (1ALD-1MLD), as shown in Figure S15 (Supporting Information). As shown in Figure S15 (Supporting Information), the optimal thickness of the (1ALD-1MLD) alloy interface for Li-metal anode in the carbonate-based electrolyte is Li@(1ALD-1MLD)50. Compared to the optimal thickness for the Na-metal anode, it requests a much thicker interface layer for the Li-metal anode in the carbonate-based electrolyte. With the optimized thickness, we further investigate the structures from alloy to nano-laminated for Li-metal anode, as shown in Figure S16 (Supporting Information). We observe that the alloy structure of (2ALD-2MLD)25 presents the best cycling stability compared with the nano-laminated structures. It is worth mentioning that when the structure of the interface tunes from alloy (2ALD-2MLD) to more nano-laminated (5ALD-5MLD and 10ALD-10MLD), the electrochemical performance is even worse, which is consistence with the electrochemical performances for Na-metal anode. However, the optimized alloy structures and interface thicknesses for both Li- and Na-metal anodes are different, which should be the results led by the balances of chemical/electrochemical/mechanical properties in different electrolytes. The comparison of the electrochemical performances for bare Li foil and Li@(2ALD-2MLD)25 is shown in Figure 2d–f. With the current density of 2 mA cm^{-2} and the capacity of 1 mAh cm^{-2}, the overpotential of bare Li start to fluctuate after 150 h with the overpotential increasing from 100 to 800 mV. After 270 h, the short circuit happens for the bare Li foil. However, for the Li@(2ALD-2MLD)25, the cell is very stable with the overpotential of 80 mV over 500 h. When increasing the current density to 3 and 5 mA cm^{-2} (Figure 2e,f), the Li(2ALD-2MLD)25 displays significantly improved electrochemical performances with low overpotential and longer lifetime compared to the bare Li foil without coatings.

To understand the influence of the Al_2O_3–alucone alloy interface on the Na deposition behavior, the morphology and surface composition of Na metal was investigated by different characterizations. **Figure 3** and Figures S17, S18 (Supporting Information) show the SEM images of bare Na foil and Na@(1ALD-1MLD)10 after electrochemical cycling of 50 cycles and long cycles at the current density of 1 mA cm^{-2} with a capacity limit of 1 mAh cm^{-2}. From Figure 3a and Figure S17 (Supporting Information), we can observe that mossy Na and dead Na layers are formed within 50 cycles, becoming more significant after longer cycling. With long electrochemical cycles (Figure S17, Supporting Information), long and deep cracks are formed with a rougher surface on the Li, which causes the increase of polarization in the cells and eventually leads to the short-circuit of the batteries. On the contrary, the morphologies of the Na@(1ALD-1MLD)10 after cycling are different, as shown in Figure 3b and Figure S18 (Supporting Information). The surfaces of the Na@(1ALD-1MLD)10 are much smoother with less mossy Na and crack formation after 50 cycles and long cycles. The mossy/dendritic Na growth and dead Na formation are effectively prevented with the Al_2O_3–alucone alloy interfaces, which leads to significantly improved electrochemical performances. To further study the Na deposition behavior, the Cu foils (with and without coating) are used as working electrodes. Figure S19 (Supporting Information) shows the SEM images of bare Cu foil and Cu@(1ALD-1MLD)10 with electrochemical deposition of different capacities of 0.1 and 1 mAh cm^{-2} at the current density of 1 mA cm^{-2}. It can be clearly seen from Figure S19a (Supporting Information) that the morphology of the deposited Na on bare Cu foil during the initial nuclear process with the capacity of 0.1 mAh cm^{-2} is non-uniform with mossy Na and crack formation. With an increasing capacity to 1 mAh cm^{-2}, the surface of the deposited Na turns rougher and large holes/cracks form during the deposition process. On the contrary, the Na deposition on the Cu@(1ALD-1MLD)10 is very smooth without any mossy and dendrite formation from the nuclear stage to the higher capacity, as shown in Figure S19b (Supporting Information). The deposition behavior study demonstrates that the designed nanoalloy interface is enabled to reduce the Na-dendrite growth and is expected to improve the electrochemical performances.

Besides the morphology, the compositions of the interface are critical for the metal deposition and electrochemical performances. The TOF-SIMS is carried out to understand the chemical composition of the interface after plating/stripping. In

© 2023 Wiley-VCH GmbH

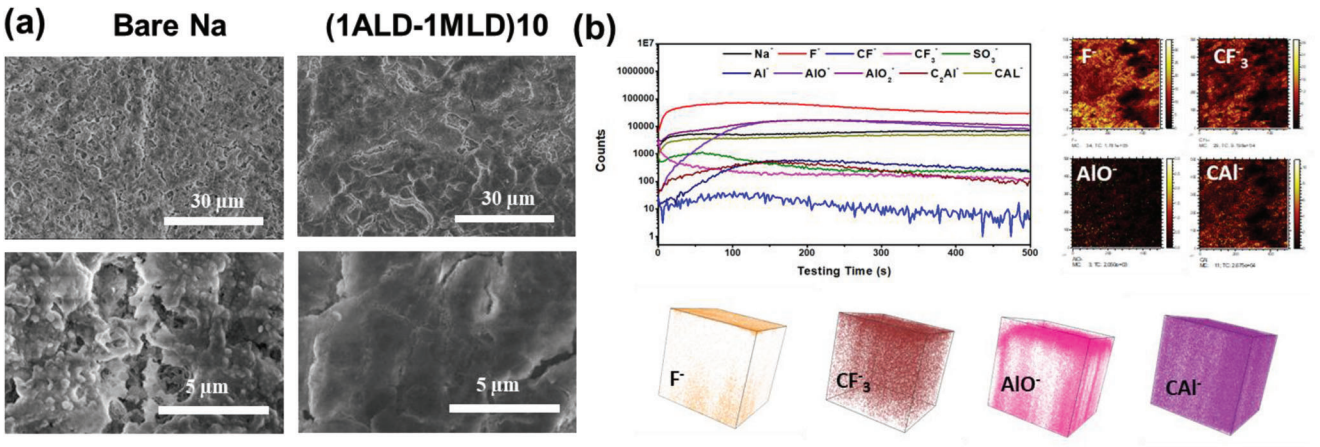

Figure 3. a) Top-view SEM images of bare Na foil and Na@(1ALD-1MLD)10 after electrochemical cycling (50 cycles). b) TOF-SIMS depth profiles and corresponding 3D reconstructed images of Na@(1ALD-1MLD)10 after electrochemical cycling.

Figure S20 (Supporting Information), the TOF-SIMS results of surface chemical ion images, depth profiles, and corresponding 3D reconstructed images for bare Na foil after 50 cycles of plating/stripping under the conditions of 1 mA cm^{-2}/1 mAh cm^{-2} are displayed. For cycled bare Na foil (Figure S20, Supporting Information), the surface is covered with by-products from the side reactions between Na metal with electrolytes, presenting the strong signal of F^- and SO_3^-. As shown in Figure 3b, the Al_2O_3–alucone alloy coating remains on the surface of Na metal after cycling and has small changes compared to the TOF-SIMS result before cycling (Figure 1b). The TOF-SIMS results demonstrate that the Al_2O_3–alucone alloy interface is robust and chemical/electrochemical stable during electrochemical cycling. Similarly, the TOF-SIMS results for bare Li foil and Li@(1ALD-1MLD)50 after 50 cycles of electrochemical plating/stripping are presented in Figures S21, S22 (Supporting Information), respectively. The pristine Li shows deep penetration of F from electrolyte with a long sputtering time (over 1000 s), which is related to the thick dead Li layer formation. In contrast, for the Li@(1ALD-1MLD)50 after cycling (Figure S22, Supporting Information), the Al_2O_3–alucone alloy interface is very stable and remains with a similar structure compared to the coating before cycling. The XAS at Al K-edge was performed for Li@(2ALD-2MLD)25 after cycling. After cycling, the XAS spectra of Al K-edge (Figure S23, Supporting Information) become broader, with the peak shifts to higher energy compared to that of before cycling. However, it still confirms that the (2ALD-2MLD)25 interface is a stable protective layer during cycling. The integration of organic compounds, such as zincone and titanicone, into inorganic layers can lead to the formation of polymer chains containing benzene rings, specifically $(–Zn–O–Benzene–O)_n$ and $(–Ti–O–Benzene–O)_n$.[19] DFT calculations have shown that these polymer chains are the key to reducing the energy barrier for Li-ion migration.[19] Similarly, in this work, the addition of the alucone organic layer expectedly containing $(–Al–O–CH_x–O)_n$ chains could have similar potential to enhance Li- and Na-ion migration at the interface.

We further investigated the influence of mechanical properties on the interfaces. First, we understand the effect of the thickness of the film on the mechanical properties using the 1ALD-1MLD alloy structure as an example. The mechanical performance of the different film thicknesses of 1ALD-1MLD alloy structures was evaluated using the AFM deflection technique where the center of a free-standing film is deflected with a predefined force and the film deflection from the applied force is detected.[9a,c,20] A holey silicon nitride TEM grid with a hole diameter of 2.7 μm covered with monolayer graphene as a support layer was used to deposit the ALD and MLD films. The mechanical properties of single-layer graphene were found to dominate the mechanical performance of thin layers up to 3 nm thickness, therefore we evaluated the mechanical performance of (1ALD-1MLD)10 and (1ALD-1MLD)25 and (1ALD-1MLD)50 with 4–20 nm thickness. All mechanical tests were conducted using an Asylum MFP-3D AFM. The cantilever with a diamond tip (NadiaProbes, Catalogue #: ND-DYIRS-5) was calibrated using Sader's method with a normal spring constant of 35 N m^{-1}. For elastic studies, the films were deflected to small force ranges <60 nN while the films were deflected to failure at higher force levels to study the failure. At least ten samples were collected for elastic and failure behavior for each film. For all of the films, the elastic response was found to be consistent and repeatable. No significant hysteresis was observed between loading-unloading curves, implying no obvious slippage between deposited layers and graphene substrate. Due to the covalent bonding inherent to the deposition process, good adhesion between ALD and MLD layers is expected, and no hysteresis was observed for deflection tests. Figure S24 (Supporting Information) represents the elastic behavior of the (1ALD-1MLD)10 and (1ALD-1MLD)25 and (1ALD-1MLD)50 films. As expected, the in-plane stiffness of the alloy structure increased with the thickness (stiffness is related to the slope of the force-deflection curve). The films deflected to failure which is identified by abrupt force drop to or beyond 20% of maximum force. Failure force–deflection representative curves of the (1ALD-1MLD)10 and (1ALD-1MLD)25 and (1ALD-1MLD)50 alloy films are shown in Figure S24b (Supporting Information). The elastic and failure results showed that the (1ALD-1MLD)50 remains stiff, from the slope of the (F–δ) curve, during the entire loading stage to failure. Interestingly, for (1ALD-1MLD)10 and (1ALD-1MLD)25 films the slope of the F–δ curve was observed to significantly increase at higher forces and as such the film

© 2023 Wiley-VCH GmbH

exhibited higher stiffness. The increased stiffness is likely due to strain hardening from the alignment of the polymer network in the (1ALD-1MLD) alloy during plastic deformation which is noticeable for smaller thicknesses. The toughness values of the films were calculated based on the area under the F–δ curve below the failure point. In Figure S24c (Supporting Information), the F_{Facture} and toughness values of the alloy structures normalized to the film thinness are presented. The trend in the normalized F_{Fracture} and toughness to thickness implies that a higher amount of force is required to fail the thinner films; therefore, the normalized toughness decreases with thickness due to the higher volume and higher number of defects under the tip at failure. These mechanical results indicate that the thinner films with higher toughness likely will fail under higher stress levels and can show more flexibility at the interface with Na compared to thicker films, which is in agreement with their electrochemical performances in this work.

We further used the same AFM deflection technique mentioned before to study the mechanical performance of (1ALD-1MLD)50, (2ALD-2MLD)25 alloy film, and (5ALD-5MLD)10 nano-laminated film with a similar thickness of ≈20 nm, which are used as protective layers for Li-metal anodes (As shown in Figure S25, Supporting Information). As discussed above, for the Li-metal anode, the optimized thickness and composition for electrochemical performance are (2ALD-2MLD)25. Interestingly, when increasing the film thicknesses to 20 nm, the mechanical performances of the films from the alloy structure to the nano-laminated structure are not as strong as the films with a thin thickness (like 4 nm), which is likely due to the increased volume of the films as well as the number of defects under the AFM tip. However, the nanoalloy structure of (2ALD-2MLD)25 still presents higher forces and higher stiffness compared to the other two films, which is constant with the electrochemical performances of the Li-metal anode. Herein, although the optimized thicknesses and compositions for Li and Na metals are quite different, the mechanical properties still play an important role in affecting the electrochemical stabilities.

As observed in the previous section, the optimal thickness of SEI for Li is 20 nm, while it is 4 nm for Na. This section aims to explain why Li needs a thicker SEI layer to effectively suppress dendrites. To do so, the mechanics of the SEI delamination is simulated with a cohesive zone model (CZM). **Figure 4**a shows the geometry and initial/boundary conditions of the stress equilibrium equation. The initial damage area refers to the region where the SEI is fully delaminated from the anode surface due to the Li/Na-dendrite initiation and is under mechanical pressure from Li/Na-dendrite nucleation pushing outward. The undamaged area is modeled by CZM with the bilinear form of traction-separation law[21] (Supporting Information for more details). The physics simulation is run in, a finite element software, COMSOL Multiphysics. The magnitude of pressure that Li/Na acting on the SEI is evaluated through the following thermodynamics relationship:[22]

$$\sigma V_{\text{m}} = F\Delta\emptyset \tag{1}$$

where σ is mean stress, V_{m} is the molar volume of the anode, F is the Faraday constant, and $\Delta\emptyset$ is the overpotential that drives the reaction. Under the same charging rate, $\Delta\emptyset$ is assumed constant, and thus the mechanical pressure is solely a function of V_{m}, which varies from one to another material. Experimental characterizations, Figure S26 (Supporting Information), show that under the same charging conditions (3 mA cm^{-2}, 5 mAh cm^{-2}), the thickness ratio of deposited Li over the deposited Na (V_{m},Li/$V_{\text{m,Na}}$) is 0.59. Therefore, the ratio of pressure exerted by deposited Na and Li ($\sigma_{\text{Li}}/\sigma_{\text{Na}}$) is 1.82. Here, in the simulation, it is assumed that σ_{Li} is 100 MPa; thus, σ_{Na} is 59 MPa. The studied range of SEI thickness is from 4 to 20 nm. The displacement of the left boundary in the y-direction is associated with the dendrite length and is measured when the system reaches mechanical equilibrium. Figure 4b shows that when the SEI thickness is 4 nm, the Li-dendrite length is much larger than the Na dendrite. And to achieve a similar suppression performance (same length of dendrites), Li would obviously require a thicker SEI than Na due to a larger induced mechanical stress.

Next, we aim to simulate how each (1ALD-1MLD) thickness works against dendrite nucleation through the phase-field model for dendrites coupled with SEI mechanics. This phase-field model is an extension of Chen and antratian's works.[23] More details are available in Supporting Information. Figure 4c shows the initial morphology of the anode surface with a perturbation radius of 4 nm. In this mechano-electrochemical modeling, the velocity of the moving Li/SEI interface is the boundary condition that causes the stress distribution in the SEI domain. Meanwhile, the interfacial stress at Li/SEI interface plays a part in controlling the plating behavior: interfacial tensile stress promotes deposition rate, while interfacial compressive stress suppresses deposition reaction. Each (1ALD-1MLD) thickness has distinct mechanical properties due to the size scale effect, and the elastic modulus of each one is extracted from Figure S24 (Supporting Information). The negative overpotential of 0.1 V is applied to simulate plating behavior. Stress distributions in the SEI, as well as the resulting surface morphologies, are captured at the end of the simulations.

Figure 4e shows how different SEI thicknesses smoothen the anode surface during the plating process. The black line represents the initial anode surface, with one perturbation. As a result of plating, the final anode surface rises up, but the morphologies are different from one to another case. (1ALD-1MLD)25, and (1ALD-1MLD)50 both result in a very smooth surface, while the perturbation is not well suppressed in the case of (1ALD-1MLD)10. This is due to the different magnitudes of mechanical stress at the interface, Figure 4d,f. (1ALD-1MLD)25 and (1ALD-1MLD)50 possess a similar magnitude of interfacial stress, while the interfacial stress in (1ALD-1MLD)10 is lower. The mechanical suppression mechanism works by slowing down the deposition rate at the tip due to compressive stress while promoting the plating reaction at the valleys due to tensile stress. However, if the interfacial mechanical stress is too low, the impact of mechanics on the electrochemical reaction is not significant, and rough surfaces are not effectively alleviated, like in the case of (1ALD-1MLD)10. As a result, a thicker SEI layer tends to have better dendrite suppression performance. Nevertheless, it is important to note that high tensile stress at the interface can also cause SEI delamination, leading to other interfacial issues. Therefore, the thickness of the SEI layer must be optimized to balance the mechanical suppression effect and the potential delamination issue.

© 2023 Wiley-VCH GmbH

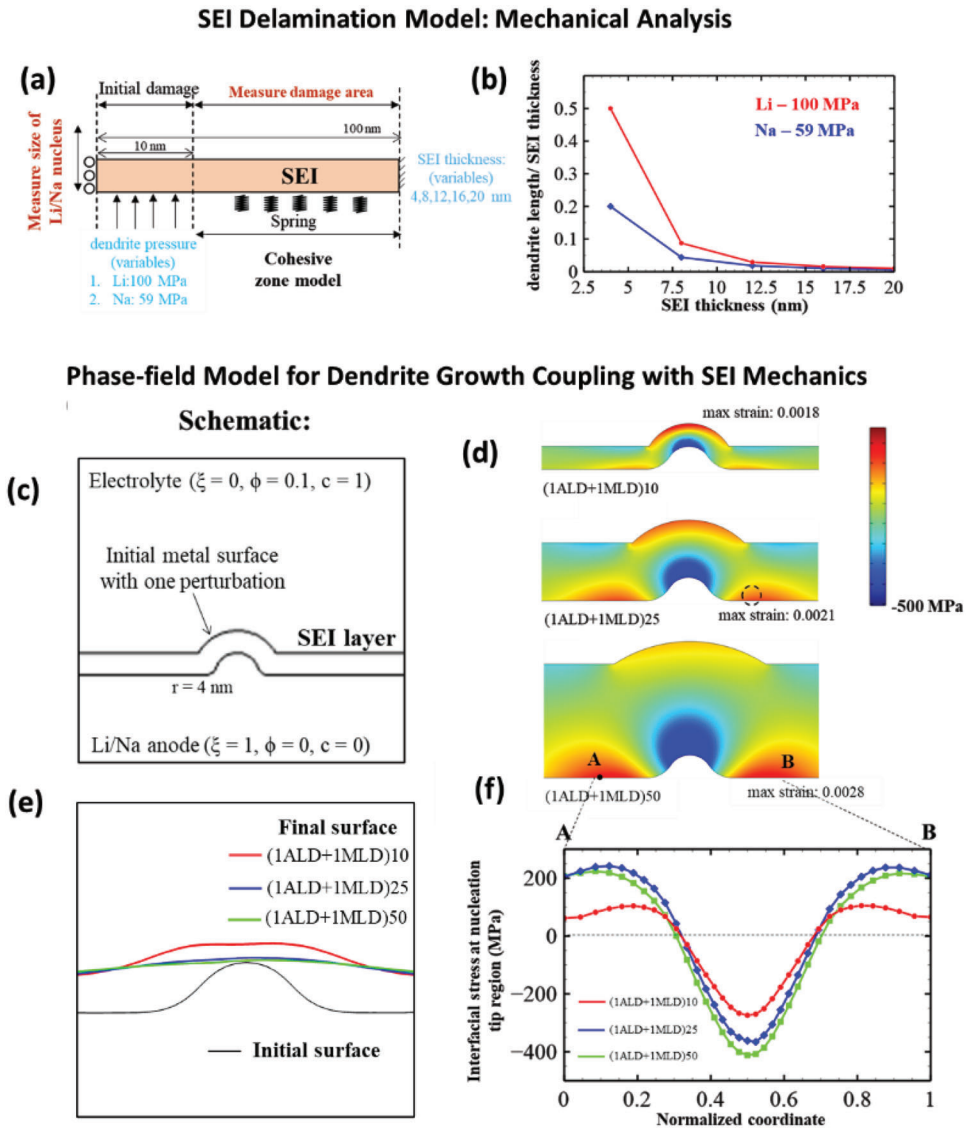

Figure 4. a,b) SEI delamination model based on mechanical analysis. a) Schematic with initial and boundary conditions. b) Plot of the SEI thicknesses against the resulting dendrite nucleation length (normalized with the SEI thicknesses). c–f) Phase-field model for dendrite growth coupling with SEI mechanics. c) Schematic of the simulation with initial and boundary conditions. d) Stress distribution on three SEI thicknesses: (1ALD-1MLD)10, (1ALD-1MLD)25, and (1ALD-1MLD)50. e) Resulting anode surfaces due to the mechanical suppression by each SEI thickness. f) 1D interfacial stress distribution near the perturbation region from point A to B.

Based on the discussion above combining electrochemical performance, mechanical property measurements, and theoretical modeling, we have provided a comprehensive understanding on the electrochemical/chemical/mechanical stability of the interfaces for metal anodes. 1) For both Li- and Na-metal anodes, the nanoalloy structure interfaces present the best electrochemical performances and the nanoalloy interfaces are electrochemically and chemically stable after cycling. 2) However, the thicknesses of the nanoalloy interfaces required for Li- and Na-metal anodes are quite different, in which a thicker interface is essential for Li metal and a thinner coating is strong enough for Na metal. A cohesive zone model is proposed to explain the mechanism. 3) The mechanical behavior of the hybrid films is affected by both thickness and configuration. Although the thin nanoalloy film demonstrates a higher toughness and average failure force, the thick nanoalloy interface provides a higher interfacial stress and smooth surface based on the phase-field modeling.

3. Conclusion

We have demonstrated a new concept of organic and inorganic hybrid interfacial layers for both Li- and Na-metal anodes. By controlling the compositions, we realize the nanoalloy structure to the nano-laminated structure. As a result, the nanoalloy interface presents the most stable electrochemical performances for both Li- and Na-metal anodes. The thicknesses of the nanoalloy interfaces required for Li- and Na-metal anodes are different and the mechanism is understood by a cohesive zone

© 2023 Wiley-VCH GmbH

model. Furthermore, the influence of the mechanical stabilities of the different interfaces on the electrochemical performances has been investigated experimentally and theoretically. Our approach provides a fundamental understanding and establishes the bridge between mechanical properties and electrochemical performance for alkali-metal anodes. In addition, a comprehensive understanding on the electrochemical/chemical/mechanical stability of the interfaces for metal anodes has been studied by combing experimental measurements and theoretical modeling. We believe that this work can not only open a new window on the design of the electrochemical/chemical/mechanical stable interfaces for alkali metal but also provides new insight into the mechanical effects of electrochemical metal depositions.

Supporting Information

Supporting Information is available from the Wiley Online Library or from the author.

Acknowledgements

P.P., K.T., and M.A. contributed equally to this work. This research was supported by the Natural Science and Engineering Research Council of Canada (NSERC), the Canada Foundation for Innovation (CFI), and the University of Western Ontario (UWO). The authors gratefully acknowledge Dr. Heng-Yong Nie for his help in the discussion on TOF-SIMS results. The authors would like to acknowledge the technical expertise of Mr. Jack Hendriks at the Western Tandetron Accelerator Facility. This research used resources of the Advanced Light Source, a DOE Office of Science User Facility under contract no. DE-AC02-05CH11231.

Conflict of Interest

The authors declare no conflict of interest.

Data Availability Statement

The data that support the findings of this study are available from the corresponding author upon reasonable request.

Keywords

alkali-metal anodes, artificial interfaces, atomic layer deposition (ALD) and molecular layer deposition (MLD), Li-metal batteries, Na-metal batteries, nano-hybrid films

Received: February 13, 2023
Revised: March 28, 2023
Published online: June 1, 2023

[1] a) Y. Ding, Z. P. Cano, A. Yu, J. Lu, Z. Chen, *Electrochem. Energy Rev.* **2019**, *2*, 1; b) Y. Zhang, T.-T. Zuo, J. Popovic, K. Lim, Y.-X. Yin, J. Maier, Y.-G. Guo, *Mater. Today* **2020**, *33*, 56.

[2] W. Yao, P. Zou, M. Wang, H. Zhan, F. Kang, C. Yang, *Electrochem. Energy Rev.* **2021**, *4*, 601.

[3] a) H. Wang, Y. Liu, Y. Li, Y. Cui, *Electrochem. Energy Rev.* **2019**, *2*, 509; b) B. Sun, P. Xiong, U. Maitra, D. Langsdorf, K. Yan, C. Wang, J. Janek, D. Schroder, G. Wang, *Adv. Mater.* **2020**, *32*, 1903891.

[4] a) C. Zhao, Y. Lu, J. Yue, D. Pan, Y. Qi, Y.-S. Hu, L. Chen, *J. Energy Chem.* **2018**, *27*, 1584; b) Y. Zhao, K. R. Adair, X. Sun, *Energy Environ. Sci.* **2018**, *11*, 2673.

[5] a) B. Sun, P. Li, J. Zhang, D. Wang, P. Munroe, C. Wang, P. H. L. Notten, G. Wang, *Adv. Mater.* **2018**, *30*, 1801334; b) F. He, W. Tang, X. Zhang, L. Deng, J. Luo, *Adv. Mater.* **2021**, *33*, 2105329; c) A. Hu, W. Chen, X. Du, Y. Hu, T. Lei, H. Wang, L. Xue, Y. Li, H. Sun, Y. Yan, J. Long, C. Shu, J. Zhu, B. Li, X. Wang, J. Xiong, *Energy Environ. Sci.* **2021**, *14*, 4115.

[6] a) D. H. Liu, Z. Bai, M. Li, A. Yu, D. Luo, W. Liu, L. Yang, J. Lu, K. Amine, Z. Chen, *Chem. Soc. Rev.* **2020**, *49*, 5407; b) H. Wang, C. Wang, E. Matios, W. Li, *Angew. Chem., Int. Ed.* **2018**, *57*, 7734.

[7] Z. Han, C. Zhang, Q. Lin, Y. Zhang, Y. Deng, J. Han, D. Wu, F. Kang, Q. H. Yang, W. Lv, *Small Methods* **2021**, *5*, 2001035.

[8] a) G. Jiang, K. Li, F. Yu, X. Li, J. Mao, W. Jiang, F. Sun, B. Dai, Y. Li, *Adv. Energy Mater.* **2020**, *11*, 2003496; b) T. Wang, Y. Hua, Z. Xu, J. S. Yu, *Small* **2022**, *18*, 2102250.

[9] a) Y. Zhao, M. Amirmaleki, Q. Sun, C. Zhao, A. Codirenzi, L. V. Goncharova, C. Wang, K. Adair, X. Li, X. Yang, F. Zhao, R. Li, T. Filleter, M. Cai, X. Sun, *Matter* **2019**, *1*, 1215; b) Z. Yu, Y. Cui, Z. Bao, *Cell Rep. Phys. Sci.* **2020**, *1*, 100119; c) Y. Sun, M. Amirmaleki, Y. Zhao, C. Zhao, J. Liang, C. Wang, K. R. Adair, J. Li, T. Cui, G. Wang, R. Li, T. Filleter, M. Cai, T. K. Sham, X. Sun, *Adv. Energy Mater.* **2020**, *10*, 2001139; d) Y. Liu, Y.-K. Tzeng, D. Lin, A. Pei, H. Lu, N. A. Melosh, Z.-X. Shen, S. Chu, Y. Cui, *Joule* **2018**, *2*, 1595.

[10] A. L. Davis, R. Garcia-Mendez, K. N. Wood, E. Kazyak, K.-H. Chen, G. Teeter, J. Sakamoto, N. P. Dasgupta, *J. Mater. Chem. A* **2020**, *8*, 6291.

[11] a) D. Wang, H. Liu, F. Liu, G. Ma, J. Yang, X. Gu, M. Zhou, Z. Chen, *Nano Lett.* **2021**, *21*, 4757; b) Y. Sun, Y. Zhao, J. Wang, J. Liang, C. Wang, Q. Sun, X. Lin, K. R. Adair, J. Luo, D. Wang, R. Li, M. Cai, T. K. Sham, X. Sun, *Adv. Mater.* **2019**, *31*, 1806541; c) Z. Xu, J. Yang, T. Zhang, L. Sun, Y. Nuli, J. Wang, S. i. Hirano, *Adv. Funct. Mater.* **2019**, *29*, 1901924; d) Z. Huang, S. Choudhury, N. Paul, J. H. Thienenkamp, P. Lennartz, H. Gong, P. Müller-Buschbaum, G. Brunklaus, R. Gilles, Z. Bao, *Adv. Energy Mater.* **2021**, *12*, 2103187.

[12] T. Krauskopf, F. H. Richter, W. G. Zeier, J. Janek, *Chem. Rev.* **2020**, *120*, 7745.

[13] a) Y. Gao, Z. Yan, J. L. Gray, X. He, D. Wang, T. Chen, Q. Huang, Y. C. Li, H. Wang, S. H. Kim, T. E. Mallouk, D. Wang, *Nat. Mater.* **2019**, *18*, 384; b) Y. Sun, C. Zhao, K. R. Adair, Y. Zhao, L. V. Goncharova, J. Liang, C. Wang, J. Li, R. Li, M. Cai, T.-K. Sham, X. Sun, *Energy Environ. Sci.* **2021**, *14*, 4085; c) Y. Zhao, G. Li, Y. Gao, D. Wang, Q. Huang, D. Wang, *ACS Energy Lett.* **2019**, *4*, 1271.

[14] a) X. Jin, T. H. Gu, N. H. Kwon, S. J. Hwang, *Adv. Mater.* **2021**, *33*, 2005922; b) O. I. Kalaoglu-Altan, B. K. Kayaoglu, L. Trabzon, *iScience* **2022**, *25*, 103825; c) H.-j. Kwon, H. Ye, Y. Baek, J. Hong, R. Wang, Y. Choi, I. Lee, C. E. Park, S. Nam, J. Kim, S. H. Kim, *Adv. Funct. Mater.* **2021**, *31*, 2009539; d) S. T. Mahmud, M. M. Hasan, S. Bain, S. T. Rahman, M. Rhaman, M. M. Hossain, M. Ordu, *ACS Mater. Lett.* **2022**, *4*, 1174.

[15] a) Y. Cao, X. Meng, A. Li, *Energy Environ. Mater.* **2020**, *4*, 363; b) Y. Zhao, X. Sun, *ACS Energy Lett.* **2018**, *3*, 899; c) Y. Zhao, L. Zhang, J. Liu, K. Adair, F. Zhao, Y. Sun, T. Wu, X. Bi, K. Amine, J. Lu, X. Sun, *Chem. Soc. Rev.* **2021**, *50*, 3889.

[16] a) B. H. Lee, V. R. Anderson, S. M. George, *Chem. Vap. Deposition* **2013**, *19*, 204; b) B. H. Lee, V. R. Anderson, S. M. George, *ACS Appl. Mater. Interfaces* **2014**, *6*, 16880; c) B. H. Lee, B. Yoon, V. R. Anderson, S. M. George, *J. Phys. Chem. C* **2012**, *116*, 3250; d) B. Yoon, B. H. Lee, S. M. George, *J. Phys. Chem. C* **2012**, *116*, 24784.

[17] a) J. W. Elam, S. M. George, *Chem. Mater.* **2003**, *15*, 1020; b) K. Gregorczyk, M. Knez, *Prog. Mater. Sci.* **2016**, *75*, 1; c) B. H. Lee, B. Yoon, A. I. Abdulagatov, R. A. Hall, S. M. George, *Adv. Funct. Mater.* **2013**, *23*, 532.

 © 2023 Wiley-VCH GmbH

[18] E. Jin, K. Tantratian, C. Zhao, A. Codirenzi, L. V. Goncharova, C. Wang, F. Yang, Y. Wang, P. Pirayesh, J. Guo, L. Chen, X. Sun, Y. Zhao, *Small* **2022**, *18*, e2203045.
[19] J. B. Fang, Y. Q. Cao, S. Z. Chang, F. R. Teng, D. Wu, A. D. Li, *Adv. Funct. Mater.* **2021**, *32*, 2109682.
[20] M. Amirmaleki, T. Cui, Y. Zhao, J. Tam, A. Goel, Y. Sun, X. Sun, T. Filleter, *Nano Lett.* **2021**, *21*, 437.
[21] K.-J. Lee, H.-J. Yang, K.-C. Chen, *Appl. Eng. Sci.* **2022**, 9, 100088.
[22] Y. He, X. Ren, Y. Xu, M. H. Engelhard, X. Li, J. Xiao, J. Liu, J. G. Zhang, W. Xu, C. Wang, *Nat. Nanotechnol.* **2019**, *14*, 1042.
[23] a) L. Chen, H. W. Zhang, L. Y. Liang, Z. Liu, Y. Qi, P. Lu, J. Chen, L.-Q. Chen, *J. Power Sources* **2015**, *300*, 376; b) K. Tantratian, H. Yan, K. Ellwood, E. T. Harrison, L. Chen, *Adv. Energy Mater.* **2021**, *11*, 2003417.

© 2023 Wiley-VCH GmbH